

Coseismic Coulomb stress changes on intraplate faults in the western Quebec seismic zone following three major earthquakes in the past century

Jeremy M. Rimando ^a, Alexander L. Peace ^a, Katsuichiro Goda ^b, Navid Sirous ^b, Philippe Rosset ^c, and Luc Chouinard ^c

^aSchool of Earth, Environment & Society, McMaster University, 1280 Main Street West, Hamilton, ON L8S 4K1, Canada; ^bDepartment of Earth Sciences, Western University, 1151 Richmond Street North, London, ON N6A 5B7, Canada; ^cDepartment of Civil Engineering, McGill University, 817 Sherbrooke Street West, Montreal, QC H3A 0C3, Canada

Corresponding author: Jeremy M. Rimando (email: rimandoj@mcmaster.ca)

Abstract

There is currently no active fault map for the intraplate western Quebec seismic zone (WQSZ) in eastern Canada, and consequently, no detailed finite-fault source models, which are critical for seismic hazard assessments in this region with a rapidly growing population. While previous numerical stress modelling studies have shown that mostly NNW–SSE to NW–SE-striking faults exhibit the highest potential for reactivation under the present-day tectonic stress field, such modelling is unable to take into account the interaction of faults and earthquakes. This study attempts to identify possible future rupture zones using Coulomb stress analysis. We explore the static stress transfer caused by the 1935 M_W 6.1 Témiscaming, 1944 M_W 5.8 Cornwall–Massena, and 2013 M_W 4.7 Ladysmith earthquakes, which are proximal to faults in the WQSZ that exhibit a relatively high reactivation potential, to determine whether these faults have an increased potential for failure. The significance of Coulomb stress changes (ΔCFS) observed on the nearby “receiver” faults varied widely. Among the events analyzed in this study, only the 1935 M_W 6.1 Témiscaming earthquake caused extensively positive ΔCFS (≥ 0.1 bar) on its receiver fault. The areal extent of the receiver fault that has been promoted to failure suggests that earthquakes with a comparable magnitude to the 1935 event can be triggered. This work is the first attempt to provide a physical basis for seismic hazard assessment input parameters in the WQSZ based on the results of numerical stress modelling.

Key words: Coulomb stress analysis, western Quebec seismic zone, intraplate seismicity, fault reactivation, seismic hazards

1. Introduction

Identifying causative faults for the recorded seismicity in the intraplate western Quebec seismic zone (WQSZ) in eastern Canada, like in most intraplate settings worldwide, has proven to be challenging due to the paucity of contemporary surface-rupturing earthquakes and due to the poor preservation of the topographic expression of active deformation (Stein 2007; McCalpin 2009). While nodal planes of well-determined focal mechanisms for earthquakes in the WQSZ have been linked to candidate structures based on their similarity in strike with nearby existing faults and lineaments, these interpretations remain speculative since definitive proof, in the form of surface rupture, has not been associated with any of the moderate-to-strong earthquakes (between M_W 5 and M_W 6.1) in this region (e.g., Bent 1996a, 1996b). While large prehistoric earthquakes cannot be ruled out, geomorphic evidence for these is lacking. The poor preservation of surface ruptures is due in part to the long return periods for earthquakes in this stable continental region of the North American plate, which experiences on

average approximately three earthquakes with a moment magnitude (M_W) > 5 every decade (NRCan 2023a).

The seismicity in the WQSZ is attributed primarily to the reactivation of pre-existing structures (Rimando and Peace 2021) under the contemporary tectonic stress field (Mazzotti and Townend 2010; Reiter et al. 2014; Snee and Zoback 2020). Previous regional numerical stress analyses (e.g., Rimando and Peace 2021) have shown that the mainly reverse/thrust faulting on mostly NW–SE striking faults in the WQSZ, as indicated by earthquake focal mechanisms, is compatible with the present-day NE–SW maximum horizontal stress orientation (S_{Hmax}) that is associated with spreading along the Mid-Atlantic Ridge (Richardson 1992). Structures that are currently being reactivated include faults and folds that are related to late Precambrian to early Paleozoic Iapetan rifting, and mechanical discontinuities related to Precambrian litho-tectonic terranes and plate boundaries (Kumarapeli 1978; Culotta et al. 1990; Rimando 1994; Rimando and Benn 2005). These structures, however, are associated with relict tectonic landforms that constitute most of the topographic relief

in the WQSZ, such as the grabens and half-grabens of the NE–SW-striking Saint Lawrence rift system (SLRS), and the NE–SW-striking Ottawa-Bonnechere (OBG) and Timiskaming grabens (TG; Fig. 1a) (Kay 1942; Lovell and Caine 1970; Lamontagne et al. 2020, and references therein)—but do not represent modern fault scarps.

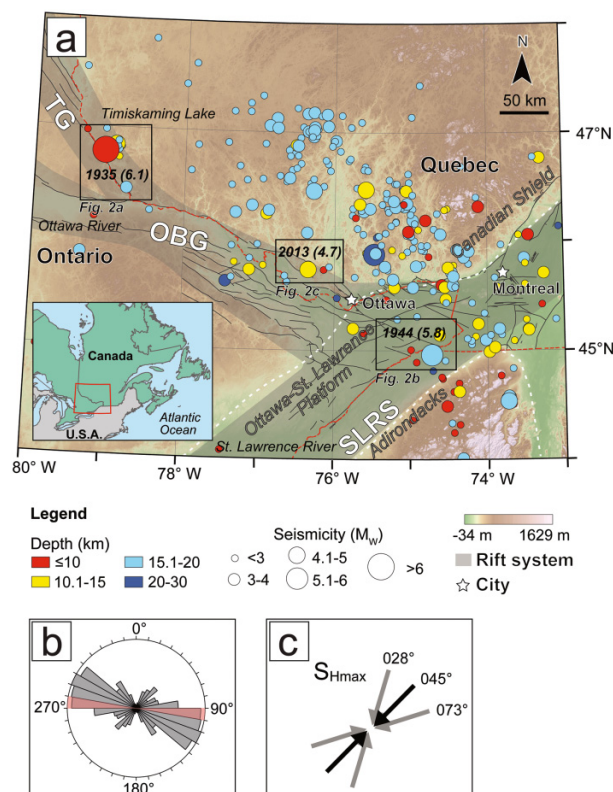
Aside from the fact that earthquakes occur infrequently in the WQSZ, the glacial and deglacial history of the region may obscure or complicate the interpretation of any evidence of recent tectonic deformation. During the Late Wisconsin deglaciation (~12 Ka), when most of the St. Lawrence was occupied by the Champlain Sea, it is likely that many single-event or cumulative deformation features may have been eroded or inundated (e.g., Dyke et al. 2002; Parent and Occhietti 2007). Where evidence of recent deformation is present, there is currently a debate whether these are due to tectonic stress or glacio-isostatic adjustment, or both (e.g., Adams 1989; Wallach et al. 1995; Brooks and Adams 2020).

Although the instrumental records of seismicity indicate the occurrence of mostly low and at most moderate-sized earthquakes in the WQSZ (NRCAN 2023b), the temporal coverage of seismicity records is too short to provide a reliable indication of the longer term level of fault activity, including return periods and the potential for large-magnitude earthquakes in the area. Globally, there is increasing evidence of large earthquakes occurring in many areas that have been previously appraised as “stable continental regions” (Calais et al. 2016; Rimando et al. 2021). The 1929 M_s 7.2 Grand Banks and the 1811–1812 M_w 7.2–8.2 New Madrid earthquakes, which occurred to the east and to the southwest of the WQSZ, respectively, are some examples of large earthquakes in eastern North America (Hasegawa and Kanamori 1987; Bent 1995; Tuttle et al. 2002). In the WQSZ itself, there is an abundance of off-fault paleoseismic evidence for possibly large-magnitude earthquakes in the not-so-distant past, mostly from the identification of seismites, such as subaqueous mass transport deposits and liquefaction features (Aylsworth and Hunter 2003; Brooks 2013, 2014, 2015; Brooks and Adams 2020).

There is a paucity of seismic, geologic, and/or geodetic data on the nature, distribution, and extent of seismogenic structures in eastern Canada, as well as earthquake size estimates, that will allow the creation of fault-source-based probabilistic seismic hazard and risk analyses of individual faults (e.g., Goda and Sharipov 2021) or seismic zones (e.g., Halchuk et al. 2014). Consequently, only areal source zone models based on historical seismicity are being utilized in the WQSZ to produce seismic hazard estimates for the National Building Code of Canada (NBCC; Halchuk et al. 2014). Current scenario-based seismic hazard and risk models in the WQSZ (e.g., Ghofrani et al. 2015; Yu et al. 2016) mainly use historical seismicity and have yet to provide physical justification for the fault source’s characteristics (location, magnitudes, and kinematics) that these utilize.

While previous numerical stress simulations have narrowed down areas for further detailed analysis (Rimando and Peace 2021), such as the long NW–SE-striking fault segments of relatively high slip tendency in the western and central portions of the WQSZ whose length would suggest a poten-

Fig. 1. (a) Map of the major tectonic features, faults, and seismicity in the western Quebec seismic zone (WQSZ) (modified from Rimando and Peace 2021). TG, Timiskaming Graben; OBG, Ottawa-Bonnechere Graben; SLRS, Saint Lawrence Rift System. The white dashed line defines the borders of the different geological provinces: the Canadian Shield, the Ottawa-St. Lawrence Platform, and the Adirondacks. The red dashed line indicates the political boundaries. The inset map, at the bottom left, shows the location of the WQSZ in eastern North America. The earthquake epicenters are coloured and scaled according to depth and magnitude. The well-localized seismicity data were derived from Adams et al. (1988, 1989), Bent (1996a), Bent et al. (2002, 2003), Du et al. (2003), Horner et al. (1978), Ma and Eaton (2007), Seeber et al. (2002), Wahlström (1987), and the earthquake bulletins of both the Natural Resources Canada (NRCAN 2023b) and the United States Geological Survey (USGS 2023). The base map is a 30 m resolution Advanced Spaceborne Thermal Emission and Reflection Radiometer global digital elevation model by NASA JPL (2023), and the fault traces are from the Geological Survey of Canada’s WQSZ faults map (Lamontagne et al. 2020). The black boxes indicate the locations of detailed maps (Fig. 2) of areas with $M_w > 4.5$ events that were investigated in this study. (b) A rose diagram summarizing the orientations of the mapped faults in the WQSZ in 18 bins (10° intervals); the red bin indicates the weighted azimuth mean. (c) A diagram of the S_{Hmax} orientations in the WQSZ, which range between 028° and 073° ; 045° is the average regional stress orientation (Mazzotti and Townend 2010). Map projection and coordinates: UTM; WGS 1984.



tial for high-magnitude earthquakes (Wells and Coppersmith 1994), such studies are unable to account for the interaction of faults and earthquakes (Wallace 1951; Bott 1959).

Coulomb stress analysis is a method that allows the examination of the effects of static stress transfer due to earthquakes on nearby faults (King et al. 1994). Coulomb stress transfer studies have been previously used to identify possible future rupture zones in an effort to improve seismic disaster mitigation (e.g., Parsons et al. 2008). Some studies immediately investigated the effects of single, recent large earthquakes on nearby faults (e.g., Parsons et al. 2008; Li et al. 2021), while some consider all the earthquakes in the historical record that are above an arbitrary magnitude threshold to systematically identify faults that have been promoted to failure (e.g., Li et al. 2020). Coulomb stress transfer studies have been carried out globally on earthquakes associated with different faulting styles in a variety of tectonic settings. Earthquake triggering on adjacent faults/fault segments by previous earthquakes has been demonstrated on well-studied fault systems associated with plate boundaries, such as the lithospheric-scale strike-slip San Andreas Fault in the USA (e.g., Stein et al. 1992; King et al. 1994) and the North Anatolian Fault in Turkey (e.g., Stein et al. 1997); the fold-and-thrust belts of Taiwan (e.g., Chan and Stein 2009; Lin et al. 2013); subduction zone megathrusts (Toda et al. 2011a); and back-arc normal faults of Italy (e.g., Walters et al. 2009).

Coulomb stress analyses in intraplate settings are less common (e.g., Mohammadi et al. 2019), and while this method has been previously applied in the nearby Charlevoix Seismic Zone in Quebec (Fereidoni and Atkinson 2015), it was done in the context of relating modern seismicity to a large historic earthquake in the 1600s and not with the goal of identifying possible future rupture zones. In this study, we analyze the Coulomb stress changes caused by seismicity in the past 100 years on nearby faults in the WQSZ, with a focus on faults that exhibit a relatively high slip tendency (Rimando and Peace 2021). The characteristics of faults that appear to be promoted to failure can provide input parameters for future scenario-based seismic hazard and risk modeling, which may have implications for urban planning, seismic design, and managing industrial operations that could alter the stress states in the area. In particular, we characterize the areal extent of the positive Coulomb stress changes associated with the events that we analyzed in this study to identify which faults exhibit an increased propensity for earthquake triggering and to explore the possible sizes of triggered earthquakes that these may host.

2. Methods and data

We focused on instrumentally recorded $M_W > 4.5$ events in the WQSZ that are proximal to mapped faults, namely the 1935 M_W 6.1 Témiscaming, 1944 M_W 5.8 Cornwall–Massena, and 2013 M_W 4.7 Ladysmith earthquakes, to examine the stress perturbations that could potentially affect nearby faults.

A change in the Coulomb failure stress (ΔCFS), caused by coseismic slip on a fault (called *source fault*, which is not to be

confused with finite-fault source models for seismic hazard assessments), can alter the state of stress in the surrounding rock volume. Positive and negative changes in the ΔCFS on nearby faults (receiver faults) have been observed to promote and inhibit failure, respectively (King et al. 1994). ΔCFS is calculated using the following equation:

$$\Delta CFS = \Delta \tau + \mu' \Delta \sigma_n$$

where $\Delta \tau$ is the change in shear stress (which is positive in the direction of fault slip), $\Delta \sigma_n$ is the change in normal stress (which is positive if the fault is unclamped), and μ' is the apparent coefficient of friction.

We utilized the MATLAB-based software, Coulomb 3.4 (Lin and Stein 2004; Toda et al. 2005), to model the coseismic static Coulomb stress changes on the receiver faults in an elastic half space (Lin and Stein 2004; Toda et al. 2005; Toda et al. 2011b). While maps of coseismic surface fault ruptures, information on detailed 3D subsurface fault geometry, and models of finite-fault slip distributions were not available, we built realistically scaled, planar source faults instead using information such as magnitude, strike, dip, and rake from focal mechanisms for the 1935 M_W 6.1 Témiscaming (Bent 1996a), 1944 M_W 5.8 Cornwall–Massena (Bent 1996b), and 2013 M_W 4.7 Ladysmith (Ma and Audet 2014) earthquakes (Table 1). Receiver faults (RF-T1; RF-C1, C2, and C3; and RF-L1; Fig. 2) were created by digitizing the faults and lineaments map compiled by the Geological Survey of Canada (Lamontagne et al. 2020). While the dip directions of these faults are known, dip values were not provided in the previous work. Thus, we assumed a dip of 60° (Table 2), which is corroborated by descriptions in previous studies of similar inherited, rift-related faults that abound the region (e.g., Lovell and Caine 1970; Rimando 1994; Rocher and Tremblay 2001).

While most previous studies assign a default coefficient of friction (μ) value of either 0.4 when μ is unknown (e.g., Stein 1999), or up to 0.8 for high-friction, low-cumulative-slip faults (Lin and Stein 2004), we used a value of $\mu = 0.5$, which is consistent with the value used in previous numerical stress modelling studies in the area (e.g., Rimando and Peace 2021) that are based on sufficiently reliable geological justifications, such as the following: 1) the prevailing knowledge that mid-crustal maximum possible differential stress ($\sigma_1 - \sigma_3$) values are most likely low in the region (e.g., Hasegawa et al. 1985; Lamontagne and Ranalli 1996, and references therein), and 2) elevated levels of pore fluid pressure associated the upward migration of mantle-derived H_2O – CO_2 -dominated fluids possibly enable the fault reactivation in eastern Canada (Sibson 1989).

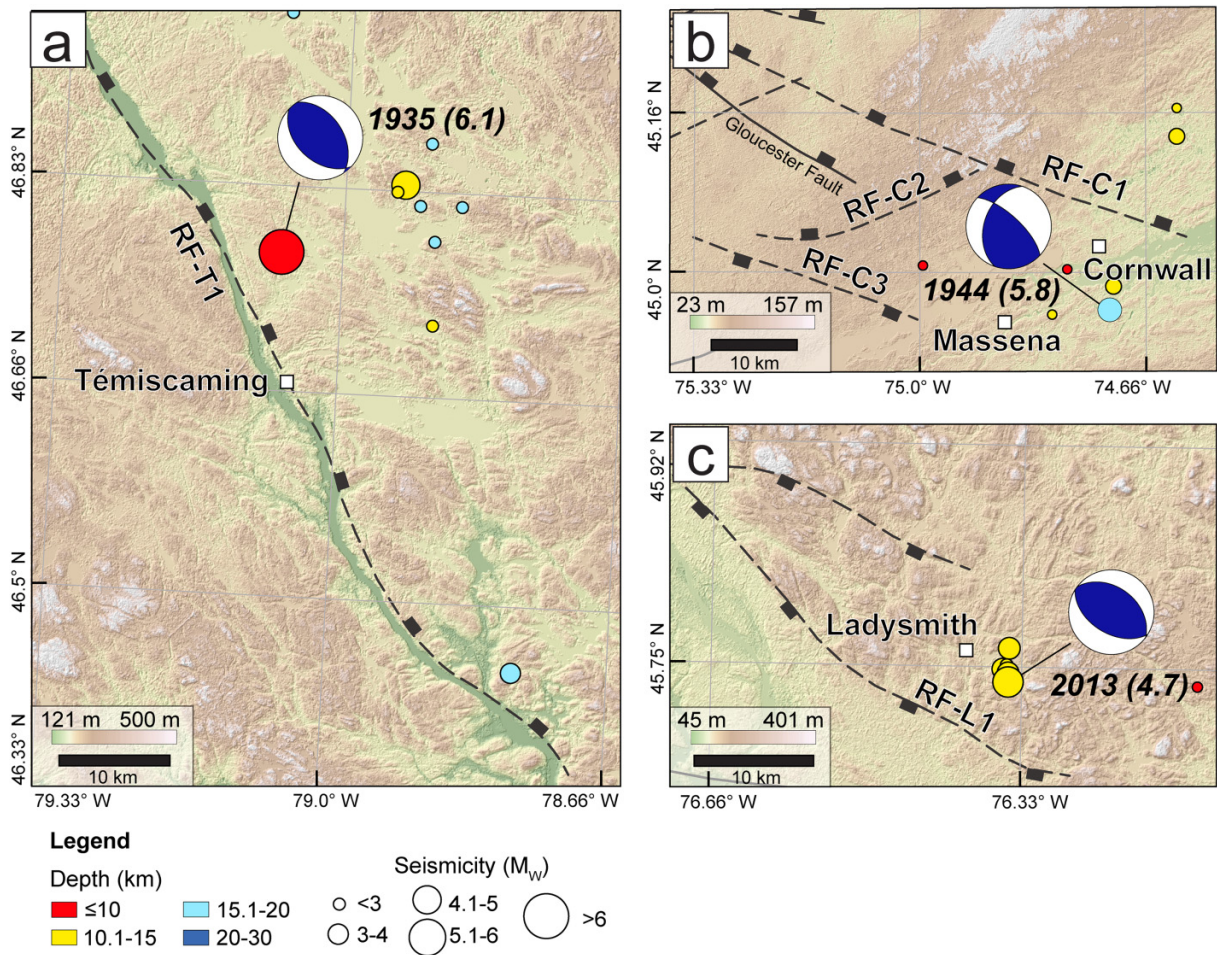
The scarcity of surface expressions, and consequently the lack of proper documentation of the kinematics of Quaternary active faults (e.g., Brooks and Adams 2020), requires determining the kinematics of possible receiver faults through other means. To determine the kinematics, we calculated the expected kinematics (expressed in rake values; Table 2) of our receiver faults using the Java-based open-source software, Slicken 1.0 (Xu et al. 2017). Input for the calculations carried out in Slicken 1.0 included the following: (1) the dip angle and direction of the receiver fault; (2) the maximum horizontal

Table 1. Source fault parameters (Data sources: [Bent \(1996a, 1996b\)](#) and [Ma and Audet \(2014\)](#)).

Date	Magnitude (M_W)	Latitude ($^{\circ}$ N)	Longitude ($^{\circ}$ E)	Depth (km)	Nodal plane 1			Nodal plane 2		
					Strike ($^{\circ}$)	Dip ($^{\circ}$)	Rake ($^{\circ}$)	Strike ($^{\circ}$)	Dip ($^{\circ}$)	Rake ($^{\circ}$)
1 November 1935	6.1	46.78	-79.07	10	130	45	80	324	46	100
5 September 1944	5.8	44.96	-74.72	20	199	42	149	313	70	52
17 May 2013	4.7	45.74	-76.35	14	306	41	94	122	50	87

Note: Rake values ($^{\circ}$) are reported following the convention of [Aki and Richards \(1980\)](#). Strike and dip values are reported following the right-hand rule.

Fig. 2. Locations of $M_W > 4.5$ earthquakes in the western Quebec seismic zone (WQSZ). These maps show plots of the focal mechanisms of $M_W > 4.5$ earthquakes, background seismicity, and nearby mapped faults. (a) The 1935 M_W 6.1 Témiscaming earthquake focal mechanism ([Bent 1996a](#)) and receiver fault, RF-T1. (b) The 1944 M_W 5.8 Cornwall–Massena earthquake focal mechanism ([Bent 1996b](#)) and receiver faults, RF-C1, C2, and C3. (c) The 2013 M_W 4.7 Ladysmith earthquake focal mechanism ([Ma and Audet 2014](#)) and receiver fault, RF-L1. The topography is derived from a 30 m resolution Advanced Spaceborne Thermal Emission and Reflection Radiometer global digital elevation model by [NASA JPL \(2023\)](#) and the fault traces are from the Geological Survey of Canada’s WQSZ faults map ([Lamontagne et al. 2020](#)). Note that the pre-existing normal faults on this map are optimally oriented for reactivation as reverse faults ([Rimando and Peace 2021](#)). Map projection and coordinates: UTM; WGS 1984.



stress directions; and (3) a stress ratio. Similar to the WQSZ fault slip tendency study by [Rimando and Peace \(2021\)](#), we assumed stress states derived from inversions of distal earthquake focal mechanisms and borehole breakouts ([Mazzotti and Townend 2010](#); [Reiter et al. 2014](#); [Snee and Zoback 2020](#)),

with an average $S_{Hmax} = 045^{\circ}$ and a stress ratio ($\phi = 1 - R = \sigma_1 - \sigma_3 / \sigma_1 + \sigma_3$) of 0.4.

While we assumed specific values for the different input parameters in modelling Coulomb stress changes, we tested the sensitivity of our models to the range of usually assumed

Table 2. Receiver fault parameters.

Receiver fault	Strike (°)	Dip (°)	Rake (°)
RF-T1	327	60	104
RF-C1	294	60	67
RF-C2	252	60	47
RF-C3	110	60	63
RF-L1	299	60	72

Note: Rake values (°) are reported following the convention of Aki and Richards (1980). Strike and dip values are reported following the right-hand rule.

values for μ (minimum $\mu = 0.4$ and maximum $\mu = 0.8$), the range of modelled receiver fault rake values based on the range of measured S_{Hmax} values in the WQSZ (minimum $S_{Hmax} = 028^\circ$ and maximum $S_{Hmax} = 073^\circ$), and a range of feasible receiver fault dip values. Since there are no independent constraints to determine which of the two nodal planes of each of the double-couple focal mechanisms represents the ruptured fault plane of each event in consideration in this study, we consider both nodal planes as possible source faults for each earthquake (Table 1).

In interpreting the Coulomb stress change modelling results in the context of increased propensity for earthquake triggering, we utilized a ΔCFS threshold of 0.1 bar (Stein 1999). Currently, there is no consensus on the Coulomb stress change threshold values that most likely cause earthquake triggering. However, Coulomb stress changes of ≥ 0.1 bar have been shown to be sufficient to promote failure and trigger seismicity on adjacent fault sections or nearby faults by an overwhelming number of studies (e.g., Reasenber and Simpson 1992; King et al. 1994; Deng and Sykes 1997; Hardebeck et al. 1998; Harris and Simpson 1998; Anderson and Johnson 1999; Stein 1999; Ziv and Rubin 2000).

3. Results

For each event, we displayed the calculated Coulomb stress changes in map view (horizontal slice at the focal depth), in cross-sectional view (across the source and receiver faults), and on the receiver fault plane itself. For each earthquake, we present the results of the “preferred model”, which assumes a $\mu = 0.5$ and an $S_{Hmax} = 45^\circ$, and we present a sensitivity analysis, which considers a range of feasible μ , receiver fault rake (based on the assumed S_{Hmax}), and receiver fault dip values (Figs. 3–5).

3.1. The 1935 M_W 6.1 Témiscaming earthquake

3.1.1. Preferred model

The map view (10 km depth slice) of Coulomb stress changes for both the SW- and NE-dipping source faults (Figs. 3a and 3d, respectively; indicated as nodal planes 1 and 2, respectively, in Table 1) of the 1935 M_W 6.1 Témiscaming earthquake shows that the NW end of the receiver fault (RF-T1) is affected the most by Coulomb stress changes, and that significant changes (≥ 0.1 bar) occur close to the surface (0 km) and up to a depth of 30 km (Figs. 3b, 3c, 3e, and 3f). Both maps exhibit roughly symmetric Coulomb

stress change patterns that are typical of dominantly reverse-slip, source–receiver fault pairs. The maps display ~ 40 km long and ~ 15 to 20 km wide NW–SE rectangular positive Coulomb stress change with central negative Coulomb stress change regions, which are spatially coincident with the map-view projections of the source faults. Both source fault model maps also show pairs of ~ 80 km long (end-to-end) NE–SW lobes of negative Coulomb stress change (Figs. 3a and 3d). In cross-sectional view (Figs. 3b and 3e), radial patterns of positive and negative Coulomb stress changes can be seen, with the source faults almost entirely exhibiting negative Coulomb stress change, except at the tips, where lobes of positive stress changes emanate. In both cross sections (Figs. 3b and 3e), the central segment of the receiver fault (RF-T1) falls within a region of negative Coulomb stress change, while the upper and lower segments of the receiver fault (RF-T1) cross regions of positive Coulomb stress change. For both source fault models, the receiver fault plane (RF-T1; Figs. 3c and 3f) exhibits a large extent of positive Coulomb stress change: ~ 40 km long, ~ 25 km wide (down-dip) doughnut-shaped regions that surround ~ 15 km long and ~ 10 to 15 km wide (down-dip) central regions of negative Coulomb stress change, which correspond to the projections of the source fault planes.

3.1.2. Sensitivity analysis

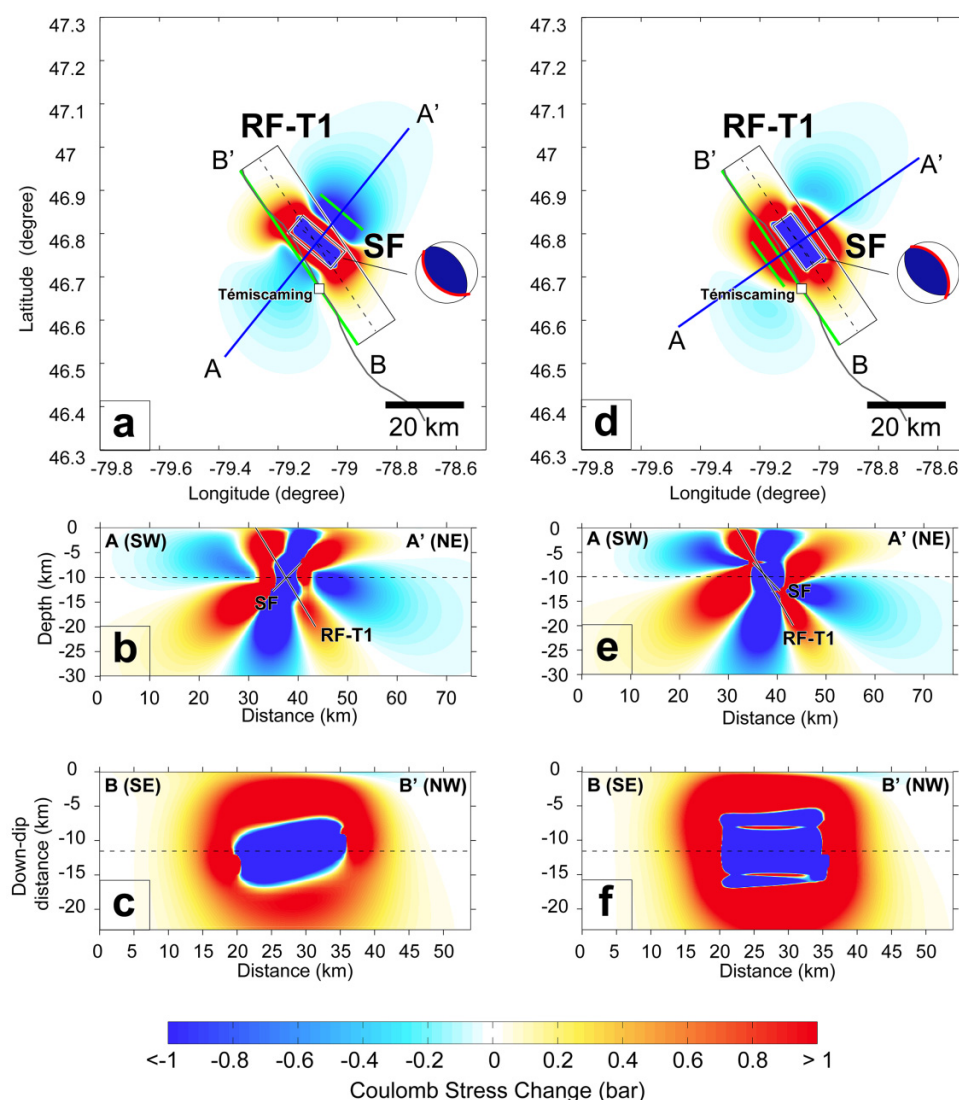
Overall, there is a minimal effect of changing the input values for μ and receiver fault rake on the Coulomb stress change distributions associated with the SW- and NE-dipping source faults, as seen in map view, in cross-sectional view, and on the receiver fault (Figs. S1–S6).

In map view (Figs. S1 and S2), a slight increase in the assumed coefficient of friction, such as between $\mu = 0.4$ and $\mu = 0.5$, has an insignificant effect on the stress change distributions. However, a larger increase in the coefficient of friction, such as between $\mu = 0.4$ and $\mu = 0.8$, appears to affect the stress change distributions more noticeably, with the Coulomb stress change distributions becoming more asymmetric and the positive and negative regions increasing and decreasing in extent, respectively, as the coefficient of friction increases. As the receiver fault rake decreases (or as the S_{Hmax} is rotated clockwise) from 121° to 72° ($S_{Hmax} = 028^\circ$ to $S_{Hmax} = 073^\circ$), the stress change patterns are rotated clockwise about an imaginary central vertical axis, which is most evident in the rotation of the lobes of negative Coulomb stress change, and the negative regions also decrease in extent.

In cross-sectional view (Figs. S3 and S4), an increase in μ and S_{Hmax} azimuth causes the stress patterns to bend/shear slightly towards the NE, and the positive (except for the lobe close to the lower portion of RF-T1) and negative regions to generally slightly increase and decrease in extent, respectively.

On the receiver fault plane (RF-T1; Figs. S5 and S6), an increase in S_{Hmax} azimuth results in clockwise shearing of the Coulomb stress change patterns (and dilation of the “slits” of positive Coulomb stress for the receiver fault of

Fig. 3. 1935 M_W 6.1 Témiscaming earthquake Coulomb stress changes. Map view (10 km depth slice) (a and d), cross-sectional view (b and e), and receiver fault (RF) plane view (c and f) of the Coulomb stress changes for the SW-dipping (a–c) and NE-dipping (d–f) source fault (SF) planes (nodal planes 1 and 2, respectively; Table 1). All calculations assumed a coefficient of friction (μ) of 0.5 and a receiver fault plane rake of 104° , based on a maximum horizontal stress value (S_{Hmax}) of 045° . Grey lines on maps represent surface fault traces, green lines represent fault surface projections, dashed black lines represent the intersection with the 10 km depth slice plane, and red lines on focal mechanisms represent the nodal plane of interest.

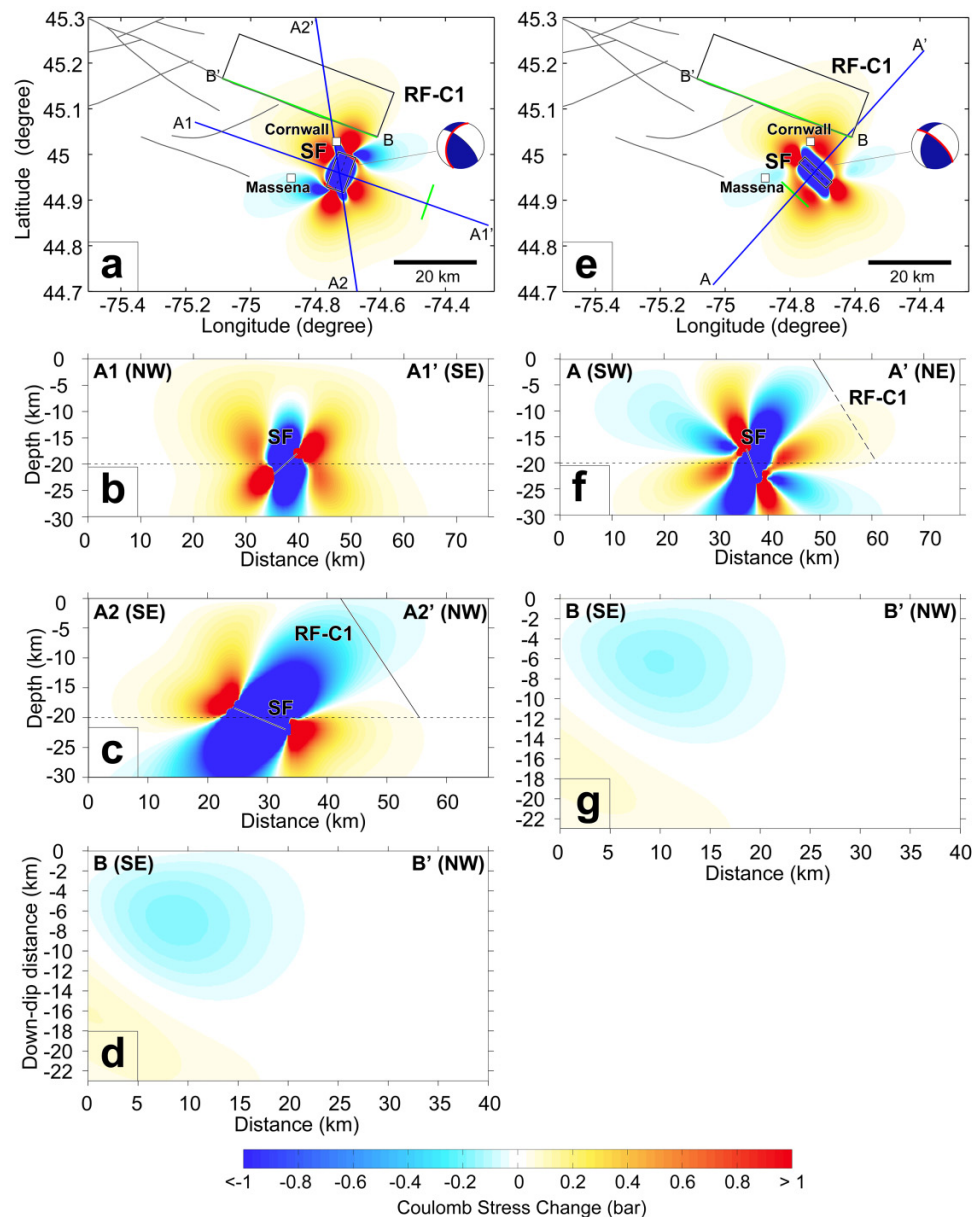


nodal plane 2 model). An increase in μ results in a slight increase in the negative Coulomb stress regions enveloping the positive Coulomb stress “doughnut” pattern associated with both source fault models and changes the morphology of the central negative Coulomb stress patches—for the receiver fault of the nodal plane 1 model, there is an increased indentation of the sides, while for the receiver fault of nodal plane 2 model, the “slits” of positive Coulomb stress shrink.

Changing the assumed receiver fault dip for this event, however, yielded more noticeable changes in stress distributions for both source fault plane models (Figs. S7 and S8). In map view, increasing the dip from 45° to 75° resulted in the counter-clockwise shearing of the stress patterns, with the

stress pattern being significantly more asymmetric and exhibiting a more pronounced increase and decrease in positive and negative regions, respectively, for the receiver fault model that assumes a dip of 75° . In cross-sectional view, an increase in dip caused the stress patterns to bend/shear slightly towards the NE and the positive and negative regions to generally slightly increase and decrease, respectively, in extent, similar to the effect of changing the μ and S_{Hmax} azimuth. On the receiver fault plane, changing the receiver fault dip resulted in significantly different downdip stress distributions. While the stress pattern changes did not exhibit any obvious trend, a significant positive Coulomb stress patch that extended for at least ~ 5 km downdip was present in all receiver fault planes.

Fig. 4. 1944 M_W 5.8 Cornwall–Massena earthquake Coulomb stress changes. Map view (20 km depth slice) (a and e), cross-sectional view (b, c, and f), and receiver fault (RF) plane view (d and g) of the Coulomb stress changes for the NW-dipping (a–d) and NE-dipping (e–g) source fault (SF) planes (nodal planes 1 and 2, respectively; Table 1). All calculations assumed a coefficient of friction (μ) of 0.5 and a receiver fault plane rake of 67° , based on a maximum horizontal stress value (S_{Hmax}) of 045° . Grey lines on maps represent surface fault traces, green lines represent fault surface projections, dashed black lines represent the intersection with the 20 km depth slice plane, and red lines on focal mechanisms represent the nodal plane of interest.



3.2. The 1944 M_W 5.8 Cornwall–Massena earthquake

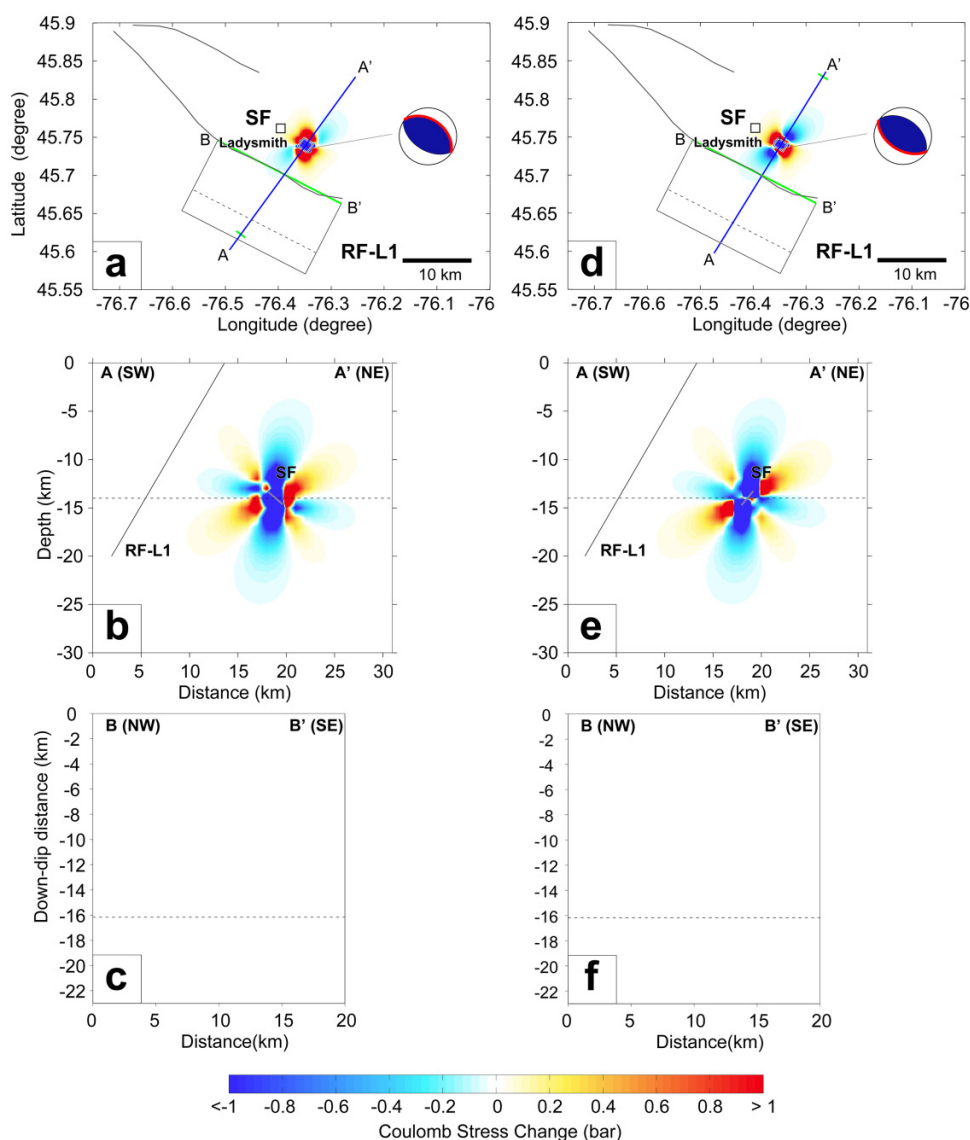
3.2.1. Preferred model

The stress changes in map view (20 km depth slice) associated with NW- and NE-dipping source faults of the 1944 M_W 5.8 Cornwall–Massena earthquake (Figs. 4a and 4e, respectively; indicated as nodal planes 1 and 2, respectively, in Table 1) appear to affect the SE end of the receiver fault (RF-C1). Both maps exhibit asymmetric Coulomb stress change

patterns that are typical of oblique reverse-slip, source-receiver fault pairs. The maps display ~50 km wide sheared clover leaf-shaped distributions of positive Coulomb stress change, with irregularly shaped centers and asymmetric paired lobes of negative Coulomb stress change (Figs. 4a and 4e) owing to the large lateral-component of slip for both the source and receiver faults (Table 1).

Cross-sectional views (Figs. 4b and 4f) of the two source fault models (perpendicular to the source fault) display different stress change patterns, with the NE-dipping source fault model having more defined radial patterns of positive

Fig. 5. 2013 M_W 4.7 Ladysmith earthquake Coulomb stress changes. Map-view (14 km depth slice) (*a* and *d*), cross-sectional view (*b* and *e*), and receiver fault (RF) plane view (*c* and *f*) of the Coulomb stress changes for the NE-dipping (*a*–*c*) and SW-dipping (*d*–*f*) source fault (SF) planes (nodal planes 1 and 2, respectively; **Table 1**). All calculations assumed a coefficient of friction (μ) of 0.5 and a receiver fault plane rake of 72° , based on a maximum horizontal stress value (S_{Hmax}) of 045° . Grey lines on maps represent surface fault traces, green lines represent fault surface projections, dashed black lines represent the intersection with the 14 km depth slice plane, and red lines on focal mechanisms represent the nodal plane of interest.



and negative Coulomb stress changes in accordance with the difference in the map-view stress change patterns between the two source fault models. Both cross sections, however, exhibit a negative Coulomb stress change over most of the source faults and lobes of positive stress change at or near the tips. A cross-sectional view through both the source and receiver faults (**Fig. 4c**) shows that the upper two-thirds of the receiver fault, RF-C1, fall within the NW lobe of negative Coulomb stress change, with the lower end of RF-C1 barely touching the NW lobe of positive Coulomb stress change.

The receiver fault planes for both source fault models (RF-C1; **Figs. 4d** and **4g**) show insignificant Coulomb stress changes (-0.1 to 0.1 bar) at the southeast end, with large (~ 20 km wide, 0 – 14 km downdip) negative Coulomb stress

change patches and smaller patches of positive Coulomb stress at the lower SE corner of the receiver fault.

3.2.2. Sensitivity analysis

There are noticeable, albeit minor, effects as a result of changing the input values for μ and S_{Hmax} on the Coulomb stress change distributions associated with the NW- and NE-dipping source faults (**Figs. S9–S14**).

In map view (**Figs. S9** and **S10**), an increase in the assumed coefficient of friction from $\mu = 0.4$ to $\mu = 0.8$ results in an increase and decrease in the extent of the positive and negative regions, respectively. As the receiver fault rake decreases (or as the S_{Hmax} is rotated clockwise), from 85° to 48°

($S_{Hmax} = 028^\circ$ to 073°), the lobes of negative Coulomb stress change become larger and distinct lobes of positive Coulomb stress change emerge.

In cross-sectional view (Figs. S11 and S12), an increase in μ results in a slight increase and decrease in the extent of the positive and negative regions, respectively, for both source models. An increase in the S_{Hmax} azimuth, causes the stress patterns to bend/shear slightly (towards the NW and the SW for the NW- and NE-dipping models, respectively), the positive regions to thin out, and the negative regions to decrease in extent, respectively.

On the receiver fault plane (RF-C1; Figs. S13 and S14), an increase in S_{Hmax} azimuth results in an increase and decrease in the extent and intensity of the negative and positive regions, respectively, for both source models. An increase in μ results causes a slight increase and decrease in the extent of the negative and positive regions, respectively, and an intensification of the negative stress regions.

The effects of changing the assumed receiver fault dip on the stress distributions for both source fault plane models of this event were substantial (Figs. S15 and S16). In map view, increasing the dip from 60° to 90° caused the map view of stress patterns to develop more distinct positive and negative lobes, with the areal extent of the negative stress changes increasing significantly as the dip approaches 90° (panels *a*, *e*, and *i* in Figs. S15 and S16). In the cross-sectional view perpendicular to the source fault, an increase in dip causes the stress patterns to bend/shear slightly towards the NW, and both the positive and negative regions to decrease in extent (panels *b*, *f*, and *j* in Figs. S15 and S16). In the cross-sectional view through both the source and receiver faults, an increase in dip caused the stress patterns to bend/shear towards the NW and both the positive and negative regions to decrease slightly in area (panels *c*, *g*, and *k* in Supplementary Figs. S15 and S16). Increasing the dip of the receiver fault plane resulted in similar patterns but more pronounced differences of magnitudes in the downdip stress distributions, with the magnitudes of the positive and negative stress regions reaching 0.4 and -0.6 bar, respectively, as the dip approached 90° (panels *d*, *h*, and *i* in Figs. S15 and S16).

We also modelled the Coulomb stress changes brought about by the 1944 M_W 5.8 Cornwall–Massena earthquake on the other mapped faults surrounding the epicenter, RF-C2 and RF-C3 (Figs. S17 and S18), but these yielded negligible Coulomb stress changes on the receiver fault, likely due to the greater distance of these faults from the hypocenter.

3.3. The 2013 M_W 4.7 Ladysmith earthquake

3.3.1. Preferred model

The map view (14 km depth slice) of Coulomb stress changes associated with the NE- and SW-dipping source faults (Figs. 5a and 5d, respectively; indicated as nodal planes 1 and 2, respectively, in Table 1) of the 2013 M_W 4.7 Ladysmith earthquake shows that the receiver fault (RF-L1) does not exhibit any Coulomb stress changes. Both maps exhibit symmetric Coulomb stress change patterns that are typical of domi-

nantly reverse-slip, source-receiver fault pairs. The maps display ~ 8 to 10 km wide positive Coulomb stress regions with central negative Coulomb stress change regions, which are roughly spatially coincident with the map-view projections of the source faults. Both source fault model maps also show pairs of ~ 10 to 12 km long (end-to-end) NE–SW lobes of negative Coulomb stress change (Figs. 5a and 5d).

In cross-sectional view (Figs. 5b and 5e), radial patterns of positive and negative Coulomb stress changes that are at least ~ 5 km perpendicular to the receiver fault can be seen, with the source faults entirely exhibiting negative Coulomb stress change, and with lobes of positive stress changes emerging at or near the tips.

For both source fault models, the receiver fault plane (RF-L1, Figs. 5c and 5f) does not exhibit any Coulomb stress changes.

3.3.2. Sensitivity analysis

In general, there are only slight effects as a result of changing the input values for μ and S_{Hmax} on the Coulomb stress change distributions associated with the NE- and SW-dipping source faults (Figs. S19–S22).

In map view (Figs. S19 and S20), an increase in the assumed coefficient of friction from $\mu = 0.4$ to $\mu = 0.8$ results in an increase and decrease in the extent of the positive and negative regions, respectively. As the receiver fault rake decreases (or as the S_{Hmax} is rotated clockwise) from 91° to 50° ($S_{Hmax} = 028^\circ$ to 073°), the lobes of negative Coulomb stress change rotate and become larger.

In cross-sectional view (Figs. S21 and S22), an increase in μ tends to rotate the stress change patterns clockwise and make the larger positive and negative lobes slightly bigger and the smaller positive and negative lobes slightly smaller for both source models. An increase in the S_{Hmax} azimuth causes the entire stress patterns to decrease in size.

Regardless of the μ and S_{Hmax} values used, there were no observed Coulomb stress changes on the receiver fault plane (RF-L1).

Noticeable changes in stress distributions for both source fault plane models were observed as a result of changing the assumed receiver fault dip for this event, albeit minimal when compared with the changes observed with the M_W 6.1 Témiscaming and 1944 M_W 5.8 Cornwall–Massena earthquakes (Figs. S23 and S24). In map view, increasing the dip from 60° to 90° resulted in the clockwise shearing of the stress patterns, with the positive stress region increasing significantly as the dip approaches 90° (panels *a*, *d*, and *g* in Figs. S23 and S24). In cross-sectional view (panels *b*, *e*, and *h* in Figs. S23 and S24), an increase in dip caused the stress patterns to bend/shear slightly towards the NE, with the positive stress region merging into a pair of larger horizontal lobes and the negative regions decreasing in extent. On the receiver fault plane, changing the receiver fault dip resulted in noticeable downdip stress distributions. At 90° dip, two small circular patches (~ 4 km diameter) of positive (>0.2 bar) and negative stress changes (<-0.2 bar) become visible (panels *c*, *f*, and *i* in Figs. S23 and S24).

4. Discussion and conclusions

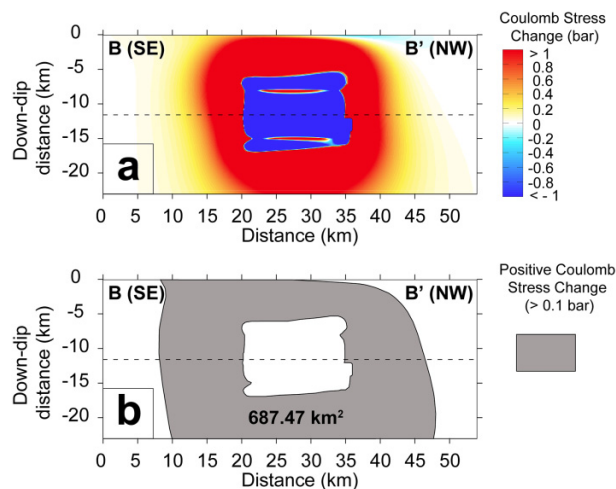
Of the three events analyzed in this study, only the 1935 M_W 6.1 Témiscaming earthquake caused extensively positive (≥ 0.1 bar) Coulomb stress changes on a nearby mapped fault (receiver fault RF-T1; Figs. 2 and 3) most likely due to the proximity of the source and receiver faults, but possibly also due to this event's relatively larger magnitude than those of the 1944 Cornwall–Massena and the 2013 Ladysmith events, as larger magnitude earthquakes redistribute tectonic stresses on faults over a much larger area (Helmstetter et al. 2005).

The positive Coulomb stress changes (≥ 0.1 bar) observed on the receiver fault, RF-T1, are extensive: ~ 40 km long (end-to-end) and ~ 25 km wide (down-dip). However, at the center of this region of positive Coulomb stress is a patch of 15 km long and ~ 10 to 15 km wide (down-dip) negative Coulomb stress changes (Fig. 3).

In the absence of documented fault surface rupture, it is currently not possible to definitively determine which of the two nodal planes most closely resembles the source fault of the 1935 M_W 6.1 Témiscaming earthquake. However, considering the similarity between the geometry and rake of the NE-dipping nodal plane of the 1935 M_W 6.1 Témiscaming earthquake focal mechanism (strike = 324° , dip = 46° , rake = 100°) and the modelled receiver fault plane, RF-T1 (average strike = 327° ; dip = 60° , rake = 104°), and considering that the dip angle of the modelled receiver fault plane was only assigned based on the known general dip of inherited normal faults in the area, it is possible that the receiver fault, RF-T1 (Figs. 2a, 3a, and 3d), and the NE-dipping nodal plane are one and the same. If this premise is true, then our calculations essentially represent the Coulomb stress changes on the source fault itself—the rectangular region of negative Coulomb stress change, therefore, represents the section of the fault that ruptured, and the positive Coulomb stress changes represent the along-strike and down-dip sections of the source fault that have been promoted to failure.

If we assume that the areal extent (km^2) of positive Coulomb stress change (≥ 0.1 bar) on the receiver fault plane (RF-T1; Figs. 3f and 6), which falls within the range of seismogenic depths of the WQSZ region, can be used to estimate the size (km^2) of future coseismic fault rupture (e.g., Shan et al. 2013; Li et al. 2021), then it is possible to estimate the possible sizes of triggered earthquake (Wells and Coppersmith 1994). The rupture of the entire donut-shaped positive Coulomb stress is unlikely, though, due to several reasons: (1) its unrealistic fault slip pattern (e.g., Mikumo et al. 1987), (2) rupture over such a large area ($\sim 700 \text{ km}^2$) would be associated with an earthquake magnitude that is much larger than that of the preceding event (a very large number of smaller earthquakes is required to trigger large earthquakes (Helmstetter 2003)), and (3) the entire area that exhibits positive Coulomb stress changes does not necessarily have to rupture—earthquakes may nucleate anywhere on the region of positive stress and rupture any fraction of its total area (Guérin-Marthe et al. 2019, and references therein), but portions of these regions of positive stress also typically host distributed smaller aftershocks

Fig. 6. Earthquake magnitude calculation example. (a) Coulomb stress changes on RF-T1 associated with the NE-dipping source fault planes (nodal plane 2; Table 1). (b) Total area of the >0.1 bar Coulomb stress change. RF, receiver fault.



that could relieve some of the stress increase (Scherbakov and Turcotte 2004; Scherbakov et al. 2005). Although unlikely, if we assume a wholesale rupture of the entire region of positive Coulomb stress change on the NE-dipping receiver fault (>0.1 bar; Fig. 6), which is associated with an area of $\sim 700 \text{ km}^2$, we can use the scaling relationship between earthquake magnitude and rupture area (Well and Coppersmith 1994) to propose an upper limit magnitude of M_W 6.9 for earthquakes triggered by the 1935 event on the receiver fault, RF-T1. There is a large gap in the seismicity data records between the 1935 M_W 6.1 Témiscaming earthquake and the present; the complete seismic bulletin data from NRCAN (2023b) is only available for 1985 onwards. Consequently, it is currently not possible to properly identify aftershocks associated with the event and analyze these with respect to the observed Coulomb stress changes. However, assuming that some of the stress increase has been relieved by aftershocks, the rupture of a smaller patch anywhere within the positively stressed region is more likely than a wholesale rupture of the entire region of positive Coulomb stress change. Therefore, a triggered earthquake with a magnitude comparable to the historical earthquake is more likely. The total area ($\sim 700 \text{ km}^2$) that exhibits positive Coulomb stress change (>0.1 bar) is large enough to host a M_W 6.1 earthquake—similar to the 1935 event, as a M_W 6.1 earthquake entails fault slip on a patch comprising only $\sim 15\%$ – 20% ($\sim 115 \text{ km}^2$) of the total area that exhibits positive Coulomb stress change ($\sim 700 \text{ km}^2$) (Well and Coppersmith 1994). While earthquakes of up to M_W 8.0 are already considered for this region in the sixth-generation seismic hazard model of Canada (Kolaj et al. 2023), establishing that other sections of RF-T1 could potentially host a M_W 6.1 earthquake provides a basis for defining a fault source model and estimating plausible earthquake magnitudes, which can be utilized in scenario seismic hazard and risk

calculations in lieu of blindly adopting historical earthquake magnitudes.

Although we were only able to explore magnitude estimates of triggered earthquakes on the receiver fault “RF-T1”, which can comprise input parameters for future seismic hazard and risk modeling in the Témiscaming area, the potential for a significant earthquake in the Cornwall–Massena and Ladysmith areas cannot be entirely ruled out, as these are obviously seismically active areas and since relatively high slip tendency values have also been measured on the NW-SE striking faults in these areas (Rimando and Peace 2021).

While we used the best data that are currently available for the different input parameters, admittedly, modelling the Coulomb stress changes of the different $>M_W$ 4.5 earthquakes in the WQSZ unavoidably incorporates epistemic uncertainties and some simplifying assumptions. One of the uncertainties pertains to the uncertainty in the magnitude, geometry, and kinematics and locations of source faults for the events that we analyzed. Despite using well-determined earthquake focal mechanisms (Bent 1996a, 1996b; Ma and Audet 2014) and accounting for the double-couple nature of these in our modelling, uncertainties that are inherent to seismic waveform inversions can also be caused by poor seismic station distribution and uncertainties in the hypothetical seismic velocity structure (e.g., Lomax et al. 2009; Karasözen and Karasözen 2020). Since data on the detailed subsurface characteristics of the faults in consideration in this study are currently unavailable (e.g., from seismic reflection profiles), we used planar source and receiver fault models from earthquake focal mechanisms and constant-dip projections of surface traces, respectively. The kinematics for both the source and receiver faults are also rather simplistic and/or hypothetical; for the source fault, in the absence of finite-fault slip models, we used rake values from earthquake focal mechanisms, and for the receiver faults, we used predicted rake values by imposing the regional stress field on the planar receiver faults.

As has been demonstrated in previous studies that analyzed the sensitivity of Coulomb stress changes to the different model input parameters (Wang et al. 2014), our sensitivity analysis shows that the Coulomb stress distributions are most sensitive to the receiver fault dip angle (Figs. S7, S8, S15, S16, S23, and S24). As higher resolution input data become available in the future, accounting for these uncertainties in our current input data may result in deviations from the stress change patterns, intensity, and locations presented in this study. However, our analysis shows that for most conceivable and geologically realistic dip scenarios for the faults in this region, the positive Coulomb stress change (≥ 0.1 bar) distributions on the receiver fault of the 1935 M_W 6.1 Témiscaming earthquake, RF-T1, consistently cover an area that is on the scale of 10^2 km² (Figs. S7 and S8), which is associated with moment magnitudes of $M_W \geq 6$ (Wells and Coppersmith 1994). Furthermore, the high slip tendency of NW-SE-striking faults in the WQSZ (Rimando and Peace 2021) corroborates our interpretation of the receiver fault “RF-T1” as a potential future rupture zone.

Acknowledgements

The authors would like to acknowledge the two anonymous reviewers and Editor-in-Chief, Dr. Brendan Murphy, for their helpful comments on an earlier version of this manuscript. We would also like to thank the Peer Review Coordinator, Ms. Katherine Kurowski, for handling our manuscript.

Article information

History dates

Received: 21 February 2023

Accepted: 30 June 2023

Accepted manuscript online: 10 July 2023

Version of record online: 14 August 2023

Copyright

© 2023 The Author(s). Permission for reuse (free in most cases) can be obtained from [copyright.com](https://creativecommons.org/licenses/by/4.0/).

Data availability

The data that support the findings of this study are available in the Supporting Information and from the following references: Bent (1996a; <https://doi.org/10.1007/BF00876667>); Bent (1996b; <https://doi.org/10.1785/BSSA0860020489>); Ma and Audet (2014; <https://doi.org/10.1139/cjes-2013-0215>); Lamontagne et al. (2020; <https://doi.org/10.4095/321900>); and Rimando et al. (2023; <https://doi.org/10.31223/X5137D>). Version 3.4 of the Coulomb Software used for the Coulomb stress analysis in this study is available at <https://www.usgs.gov/nod/e/279387>.

Author information

Author ORCIDs

Jeremy M. Rimando <https://orcid.org/0000-0003-2437-4579>

Alexander L. Peace <https://orcid.org/0000-0001-7846-3898>

Katsuichiro Goda <https://orcid.org/0000-0003-3900-2153>

Navid Sirous <https://orcid.org/0000-0003-3829-9119>

Philippe Rosset <https://orcid.org/0000-0002-7596-9196>

Luc Chouinard <https://orcid.org/0000-0002-5348-7962>

Author contributions

Conceptualization: JMR

Data curation: JMR

Formal analysis: JMR

Funding acquisition: ALP, KG, LC

Investigation: JMR

Methodology: JMR

Project administration: ALP, KG, LC

Resources: ALP, KG, LC

Software: JMR

Supervision: ALP, KG, LC

Validation: JMR, ALP, KG, NS, PR, LC

Visualization: JMR

Writing – original draft: JMR

Writing – review & editing: JMR, ALP, KG, NS, PR, LC

Competing interests

The authors declare there are no competing interests.

Funding information

JMR's postdoctoral fellowship at McMaster University was funded by the Natural Sciences and Engineering Research Council (NSERC)-Alliance grant (ALLRP 567023-21) in partnership with the Institute of Catastrophic Loss Reduction and in part by a Natural Sciences and Engineering Research Council (NSERC) Discovery Grant (RGPIN-2021-04011) awarded to ALP.

Supplementary material

Supplementary data are available with the article at <https://doi.org/10.1139/cjes-2023-0025>.

References

- Adams, J. 1989. Postglacial faulting in eastern Canada: nature, origin and seismic hazard implications. *Tectonophysics*, **163**(3–4): 323–331. doi:10.1016/0040-1951(89)90267-9.
- Adams, J., Sharp, J., and Stagg, M.C. 1988. New focal mechanisms for southeastern Canadian earthquakes (Geological Survey of Canada Open File Report 1992). p. 109. doi:10.4095/130428.
- Adams, J., Vonk, A., Pittman, D., and Vatcher, H. 1989. New focal mechanisms for southeastern Canadian earthquakes (Geological Survey of Canada Open File Report 1995). Vol. II. p. 97. doi:10.4095/130594.
- Aki, K., and Richards, P.G. 1980. Quantitative seismology: theory and methods. Vol. 859. Freeman, San Francisco, CA.
- Anderson, G., and Johnson, H. 1999. A new statistical test for static stress triggering: Application to the 1987 Superstition Hills earthquake sequence. *Journal of Geophysical Research: Solid Earth*, **104** (B9): 20153–20168. doi:10.1029/1999JB900200.
- Aylsworth, J.M., and Hunter, J.A.M. 2003. The Ottawa Valley Landslide Project: a geophysical and geotechnical investigation of geological controls on landsliding and deformation in Leda clay. Paper presented at the Third Canadian Conference on Geotechnique and Natural Hazards. *GeoHazards*. pp. 227–234.
- Bent, A.L. 1995. A complex double-couple source mechanism for the Ms 7.2 1929 Grand Banks earthquake. *Bulletin of the Seismological Society of America*, **85**(4): 1003–1020. doi:10.1785/BSSA0850041003.
- Bent, A.L. 1996a. An improved source mechanism for the 1935 Timiskaming, Quebec earthquake from regional waveforms. *Pure and Applied Geophysics*, **146**(1): 5–20. doi:10.1007/BF00876667.
- Bent, A.L. 1996b. Source parameters of the damaging Cornwall-Massena earthquake of 1944 from regional waveforms. *Bulletin of the Seismological Society of America*, **86**(2): 489–497. doi:10.1785/BSSA0860020489.
- Bent, A.L., Drysdale, J., and Perry, H.C. 2003. Focal mechanisms for eastern Canadian earthquakes, 1994–2000. *Seismological Research Letters*, **74**(4): 452–468. doi:10.1785/gssrl.74.4.452.
- Bent, A.L., Lamontagne, M., Adams, J., Woodgold, C.R., Halchuk, S., Drysdale, J., et al. 2002. The Kipawa, Quebec “Millennium” earthquake. *Seismological Research Letters*, **73**(2): 285–297. doi:10.1785/gssrl.73.2.285.
- Bott, M.H.P. 1959. The mechanics of oblique slip faulting. *Geological Magazine*, **96**(2): 109–117. doi:10.1017/S0016756800059987.
- Brooks, G.R. 2013. A massive sensitive clay landslide, Quyon Valley, southwestern Quebec, Canada, and evidence for a paleoearthquake triggering mechanism. *Quaternary Research*, **80**(3): 425–434. doi:10.1016/j.yqres.2013.07.008.
- Brooks, G.R. 2014. Prehistoric sensitive clay landslides and paleoseismicity in the Ottawa valley, Canada. *In* *Landslides in sensitive clays*. Vol. 9. Springer. pp. 119–131. doi:10.1007/978-94-007-7079-9_10.
- Brooks, G.R. 2015. An integrated stratigraphic approach to investigating evidence of paleoearthquakes in lake deposits of Eastern Canada. *Gland Surgery*, **42**(2): 247. doi:10.12789/geocanj.2014.41.063.

- Brooks, G.R., and Adams, J. 2020. A review of evidence of glacially-induced faulting and seismic shaking in eastern Canada. *Quaternary Science Reviews*, **228**: 106070. doi:10.1016/j.quascirev.2019.106070.
- Calais, E., Camelbeeck, T., Stein, S., Liu, M., and Craig, T.J. 2016. A new paradigm for large earthquakes in stable continental plate interiors. *Geophysical Research Letters*, **43**(20): 10621–10637. doi:10.1002/2016GL070815.
- Chan, C.H., and Stein, R.S. 2009. Stress evolution following the 1999 Chi-Chi, Taiwan, earthquake: consequences for afterslip, relaxation, aftershocks and departures from Omori decay. *Geophysical Journal International*, **177**(1): 179–192. doi:10.1111/j.1365-246X.2008.04069.x.
- Culotta, R.C., Pratt, T., and Oliver, J. 1990. A tale of two sutures: COCORP's deep seismic surveys of the Grenville province in the eastern US midcontinent. *Geology*, **18**(7): 646–649. doi:10.1130/0091-7613(1990)018(0646:atotsc)2.3.co;2.
- Deng, J., and Sykes, L.R. 1997. Evolution of the stress field in southern California and triggering of moderate-size earthquakes: a 200-year perspective. *Journal of Geophysical Research*, **102**(B5): 9859–9886. doi:10.1029/96JB03897.
- Du, W.X., Kim, W.Y., and Sykes, L.R. 2003. Earthquake source parameters and state of stress for the northeastern United States and southeastern Canada from analysis of regional seismograms. *Bulletin of the Seismological Society of America*, **93**(4): 1633–1648. doi:10.1785/0120020217.
- Dyke, A.S., Andrews, J.T., Clark, P.U., England, J.H., Miller, G.H., Shaw, J., and Veillette, J.J. 2002. The Laurentide and Innuitian ice sheets during the last glacial maximum. *Quaternary Science Reviews*, **21**(1–3): 9–31. doi:10.1016/S0277-3791(01)00095-6.
- Fereidoni, A., and Atkinson, G.M. 2015. Correlation between Coulomb stress changes imparted by historic earthquakes and current seismicity in Charlevoix seismic zone, eastern Canada. *Seismological Research Letters*, **86**(1): 272–284. doi:10.1785/0220140134.
- Ghofrani, H., Atkinson, G.M., Chouinard, L., Rosset, P., and Tiampo, K.F. 2015. Scenario shakemaps for Montreal. *Canadian Journal of Civil Engineering*, **42**(7): 463–476. doi:10.1139/cjce-2014-0496.
- Goda, K., and Sharipov, A. 2021. Fault-source-based probabilistic seismic hazard and risk analysis for Victoria, British Columbia, Canada: a case of the Leech River Valley Fault and Devil's Mountain Fault system. *Sustainability*, **13**(3): 1440. doi:10.3390/su13031440.
- Guérin-Marthe, S., Nielsen, S., Bird, R., Giani, S., and Di Toro, G. 2019. Earthquake nucleation size: evidence of loading rate dependence in laboratory faults. *Journal of Geophysical Research: Solid Earth*, **124**(1): 689–708. doi:10.1029/2018JB016803. PMID: 31007999
- Halchuk, S., Allen, T.I., Adams, J., and Rogers, G.C. 2014. Fifth generation seismic hazard model input files as proposed to produce values for the 2015 National Building Code of Canada. *Geological Survey of Canada, Open File*, **7576**(18): 57–123. doi:10.4095/293907.
- Hardebeck, J.L., Nazareth, J.J., and Hauksson, E. 1998. The static stress change triggering model: constraints from two southern California aftershock sequences. *Journal of Geophysical Research*, **103**(B10): 24427–24437. doi:10.1029/98JB00573.
- Harris, R.A., and Simpson, R.W. 1998. Suppression of large earthquakes by stress shadows: a comparison of Coulomb and rate-and-state failure. *Journal of Geophysical Research*, **103**(B10): 24439–24451. doi:10.1029/98JB00793.
- Hasegawa, H.S., Adams, J., and Yamazaki, K. 1985. Upper crustal stresses and vertical stress migration in eastern Canada. *Journal of Geophysical Research*, **90**(B5): 3637–3648. doi:10.1029/JB090iB05p03637.
- Hasegawa, H.S., and Kanamori, H. 1987. Source mechanism of the magnitude 7.2 Grand Banks earthquake of November 1929: double couple or submarine landslide? *Bulletin of the Seismological Society of America*, **77**(6): 1984–2004. doi:10.1785/BSSA0770061984.
- Helmstetter, A. 2003. Is earthquake triggering driven by small earthquakes? *Physical Review Letters*, **91**(5): 058501. doi:10.1103/PhysRevLett.91.058501.
- Helmstetter, A., Kagan, Y.Y., and Jackson, D.D. 2005. Importance of small earthquakes for stress transfers and earthquake triggering. *Journal of Geophysical Research*, **110**: B05S08. doi:10.1029/2004JB003286.
- Horner, R.B., Stevens, A.E., Hasegawa, H.S., and Leblanc, G. 1978. Focal parameters of the July 12, 1975, Maniwaki, Québec, earthquake—an example of intraplate seismicity in eastern Canada. *Bulletin of the Seismological Society of America*, **68**(3): 619–640. doi:10.1785/BSSA0680030619.

- Karasözen, E., and Karasözen, B. 2020. Earthquake location methods. *GEM – International Journal on Geomathematics*, **11**(1): 1–28. doi:10.1007/s13137-020-00149-9.
- Kay, G.M. 1942. Ottawa-Bonnechere graben and Lake Ontario homocline. *Geological Society of America Bulletin*, **53**(4): 585–646. doi:10.1130/GSAB-53-585.
- King, G.C., Stein, R.S., and Lin, J. 1994. Static stress changes and the triggering of earthquakes. *Bulletin of the Seismological Society of America*, **84**(3): 935–953. doi:10.1785/BSSA0840030935.
- Kolaj, M., Halchuk, S., Adams, J., and Allen, T.I. 2023. Sixth generation seismic hazard model of Canada: input files to produce values proposed for the 2020 National Building Code of Canada. Geological Survey of Canada Open-File, **8630**. doi:10.4095/331387.
- Kumarapeli, P.S. 1978. The St. Lawrence paleo-rift system: a comparative study. In *Tectonics and geophysics of continental rifts*. Springer. pp. 367–384. doi:10.1007/978-94-009-9806-3_29.
- Lamontagne, M., and Ranalli, G. 1996. Thermal and rheological constraints on the earthquake depth distribution in the Charlevoix, Canada, intraplate seismic zone. *Tectonophysics*, **257**(1): 55–69. doi:10.1016/0040-1951(95)00120-4.
- Lamontagne, M., Brouillette, P., Grégoire, S., Bédard, M.P., and Bleeker, W. 2020. Faults and lineaments of the western Quebec seismic zone, Quebec and Ontario (Open File 8361, p. 28). Geological Survey of Canada. doi:10.4095/321900.
- Li, Y., Huang, L., Ding, R., Yang, S., Liu, L., Zhang, S., and Liu, H. 2021. Coulomb stress changes associated with the M7.3 Maduo earthquake and implications for seismic hazards. *Natural Hazards Research*, **1**(2): 95–101. doi:10.1016/j.nhres.2021.06.003.
- Li, Y., Shao, Z., Shi, F., and Chen, L. 2020. Stress evolution on active faults in the southwestern Yunnan region, southeastern Tibetan Plateau, and implications for seismic hazard. *Journal of Asian Earth Sciences*, **200**: 104470. doi:10.1016/j.jseae.2020.104470.
- Lin, D.H., Chen, K.H., Rau, R.J., and Hu, J.C. 2013. The role of a hidden fault in stress triggering: stress interactions within the 1935 Mw 7.1 Hsinchu-Taichung earthquake sequence in central Taiwan. *Tectonophysics*, **601**: 37–52. doi:10.1016/j.tecto.2013.04.022.
- Lin, J., and Stein, R.S. 2004. Stress triggering in thrust and subduction earthquakes and stress interaction between the southern San Andreas and nearby thrust and strike-slip faults. *Journal of Geophysical Research*, **109**. doi:10.1029/2003JB002607.
- Lomax, A., Michelini, A., and Curtis, A. 2009. Earthquake location, direct, global-search methods. In *Encyclopedia of complexity and systems science*. Edited by R.A. Meyers. Springer, New York, NY. pp. 2449–2473. doi:10.1007/978-0-387-30440-3_150.
- Lovell, H.L., and Caine, T.W. 1970. Lake Temiskaming Rift Valley (Ontario Department of Mines miscellaneous Paper 39), p. 16. Available from <http://www.geologyontario.mndm.gov.on.ca/mndmfiles/pub/data/records/MP039.html>.
- Ma, S., and Audet, P. 2014. The 5.2 magnitude earthquake near Lady-smith, Quebec, 17 May 2013: Implications for the seismotectonics of the Ottawa-Bonnechere Graben. *Canadian Journal of Earth Sciences*, **51**(5): 439–451. doi:10.1139/cjes-2013-0215.
- Ma, S., and Eaton, D.W. 2007. Western Quebec seismic zone (Canada): clustered, midcrustal seismicity along a mesozoic hot spot track. *Journal of Geophysical Research*, **112**(B6). doi:10.1029/2006JB004827.
- Mazzotti, S., and Townend, J. 2010. State of stress in central and eastern North American seismic zones. *Lithosphere*, **2**(2): 76–83. doi:10.1130/L65.1.
- J.P. McCalpin (Editor). 2009. *Paleoseismology*. 2nd ed. International Geophysics Series. Academic Press. p. 613
- Mikumo, T., Hirahara, K., and Miyatake, T. 1987. Dynamical fault rupture processes in heterogeneous media. *Tectonophysics*, **144**(1-3): 19–36. doi:10.1016/0040-1951(87)90006-0.
- Mohammadi, H., Quigley, M., Steacy, S., and Duffy, B. 2019. Effects of source model variations on Coulomb stress analyses of a multi-fault intraplate earthquake sequence. *Tectonophysics*, **766**: 151–166. doi:10.1016/j.tecto.2019.06.007.
- NASA JPL. 2023. Retrieved January 10, 2023, from <https://asterweb.jpl.nasa.gov/>
- NRCan. 2023a. Earthquake zones in eastern Canada. Available from <http://earthquakescanada.nrcan.gc.ca/zones/eastcan-en.php#WQSZ> [accessed 15 January 2023].
- NRCan. 2023b. Earthquakes Canada. Available from <https://earthquakescanada.nrcan.gc.ca/index-en.php> [accessed 15 January 2023].
- Parent, M., and Occhietti, S. 2007. Late Wisconsinan deglaciation and Champlain Sea invasion in the St. Lawrence valley, Québec. *Great Plains Quarterly*, **42**(3): 215–246. doi:10.7202/032734ar.
- Parsons, T., Ji, C., and Kirby, E. 2008. Stress changes from the 2008 Wenchuan earthquake and increased hazard in the Sichuan basin. *Nature*, **454**(7203): 509–510. doi:10.1038/nature07177. PMID: 18600260.
- Reasenber, P.A., and Simpson, R.W. 1992. Response of regional seismicity to the static stress change produced by the Loma Prieta earthquake. *Science*, **255**(5052): 1687–1690. doi:10.1126/science.255.5052.1687. PMID: 17749422.
- Reiter, K., Heidbach, O., Schmitt, D., Haug, K., Ziegler, M., and Moek, I. 2014. A revised crustal stress orientation database for Canada. *Tectonophysics*, **636**: 111–124. doi:10.1016/j.tecto.2014.08.006.
- Richardson, R.M. 1992. Ridge forces, absolute plate motions, and the intraplate stress field. *Journal of Geophysical Research*, **97**(B8): 11739–11748. doi:10.1029/91JB00475.
- Rimando, J.M., and Peace, A.L. 2021. Reactivation potential of intraplate faults in the western Quebec seismic zone, eastern Canada. *Earth and Space Science*, **8**: e2021EA001825. doi:10.1029/2021EA001825.
- Rimando, J.M., Peace, A., Goda, K., Sirous, N., Rosset, P., and Chouinard, L. 2023. Coseismic Coulomb stress changes on intraplate faults in the western Quebec seismic zone, Canada: implications for seismic hazards. *ArXiv*. doi:10.31223/X5137D.
- Rimando, J.M., Schoenbohm, L.M., Ortiz, G., Alvarado, P., Venerdini, A., Owen, L.A., et al. 2021. Late quaternary intraplate deformation defined by the Las Chacras Fault Zone, west-Central Argentina. *Tectonics*, **40**: e2020TC006509. doi:10.1029/2020TC006509.
- Rimando, R.E. 1994. Tectonic framework and relative ages of structures within the Ottawa-Bonnechère Graben. M.Sc. thesis, University of Ottawa. Available from <https://ruor.uottawa.ca/handle/10393/10346>.
- Rimando, R.E., and Benn, K. 2005. Evolution of faulting and paleo-stress field within the Ottawa graben, Canada. *Journal of Geodynamics*, **39**(4): 337–360. doi:10.1016/j.jog.2005.01.003.
- Rocher, M., and Tremblay, A. 2001. L'effondrement de la plate-forme du Saint-Laurent: Ouverture de l'apetous ou de l'Atlantique? Apport dela reconstitution des paléocontraintes dans la région de Québec (Canada). *Comptes Rendus de l'Académie des Sciences - Series IIA - Earth and Planetary Science*, **333**: 171–178. doi:10.1016/S1251-8050(01)01610-X.
- Seeber, L., Kim, W.Y., Armbruster, J.G., Du, W.X., Lerner-Lam, A., and Friberg, P. 2002. The 20 April 2002 Mw 5.0 earthquake near Au Sable Forks, Adirondacks, New York: a first glance at a new sequence. *Seismological Research Letters*, **73**(4): 480–489. doi:10.1785/gssrl.73.4.480.
- Shan, B., Xiong, X., Wang, R., Zheng, Y., and Yang, S. 2013. Coulomb stress evolution along Xianshuihe-Xiaojiang Fault System since 1713 and its interaction with Wenchuan earthquake, May 12, 2008. *Earth and Planetary Science Letters*, **377–378**: 199–210. doi:10.1016/j.epsl.2013.06.044.
- Shcherbakov, R., and Turcotte, D.L. 2004. A damage mechanics model for aftershocks. *Pure and Applied Geophysics*, **161**: 2379–2391. doi:10.1007/s00024-004-2570-x.
- Shcherbakov, R., Turcotte, D.L., and Rundle, J.B. 2005. Aftershock statistics. *Pure and Applied Geophysics*, **162**: 1051–1076. doi:10.1007/s00024-004-2661-8.
- Sibson, R.H. 1989. High-angle reverse faulting in northern New Brunswick, Canada, and its implications for fluid pressure levels. *Journal of Structural Geology*, **11**(7): 873–877. doi:10.1016/0191-8141(89)90104-1.
- Snee, J.E.L., and Zoback, M.D. 2020. Multiscale variations of the crustal stress field throughout North America. *Nature Communications*, **11**(1): 1–9. doi:10.1038/s41467-020-15841-5. PMID: 31911652
- Stein, R.S. 1999. The role of stress transfer in earthquake occurrence. *Nature*, **402**(6762): 605–609. doi:10.1038/45144.
- Stein, R.S., Barka, A.A., and Dieterich, J.H. 1997. Progressive failure on the North Anatolian fault since 1939 by earthquake stress triggering. *Geophysical Journal International*, **128**(3): 594–604. doi:10.1111/j.1365-246X.1997.tb05321.x.
- Stein, R.S., King, G.C.P., and Lin, J. 1992. Change in failure stress on the San Andreas and surrounding faults caused by the 1992 M= 7.4

- Landers earthquake. *Science*, **258**: 1328–1332. Available from <https://www.science.org/doi/abs/10.1126/science.258.5086.1328>. doi:10.1126/science.258.5086.1328. PMID: 17778356.
- Stein, S. 2007. Approaches to continental intraplate earthquake issues. In *Continental intraplate earthquakes: science, hazard, and policy issue*. Vol. 425. Geological Society of American Spectrum Paper. pp. 1–16. doi:10.1130/2007.2425(01).
- Toda, S., Lin, J., and Stein, R.S. 2011a. Using the 2011 Mw 9.0 off the Pacific coast of Tohoku Earthquake to test the Coulomb stress triggering hypothesis and to calculate faults brought closer to failure. *Earth, Planets and Space*, **63**: 725–730. doi:10.5047/eps.2011.05.010.
- Toda, S., Stein, R.S., Richards-Dinger, K., and Bozkurt, S.B. 2005. Forecasting the evolution of seismicity in Southern California: animations built on earthquake stress transfer. *Journal of Geophysical Research*, **110**: B05S16. doi:10.1029/2004JB003415.
- Toda, S., Stein, R.S., Sevilgen, V., and Lin, J. 2011b. Coulomb 3.3 graphic-rich deformation and stress-change software for earthquake, tectonic, and volcano research and teaching—user guide. US Geological Survey Open-file Report, **1060**(2011): 63.
- Tuttle, M.P., Schweig, E.S., Sims, J.D., Lafferty, R.H., Wolf, L.W., and Haynes, M.L. 2002. The earthquake potential of the New Madrid seismic zone. *Bulletin of the Seismological Society of America*, **92**(6): 2080–2089. doi:10.1785/0120010227.
- USGS. 2023. Earthquakes. Available from <https://www.usgs.gov/natural-hazards/earthquake-hazards/earthquakes> [accessed 15 January 2023].
- Wahlström, R. 1987. Focal mechanisms of earthquakes in southern Quebec, southeastern Ontario, and northeastern New York with implications for regional seismotectonics and stress field characteristics. *Bulletin of the Seismological Society of America*, **77**(3): 891–924. doi:10.1785/BSSA0770030891.
- Wallace, R.E. 1951. Geometry of shearing stress and relation to faulting. *Journal of Geology*, **59**(2): 118–130. doi:10.1086/625831.
- Wallach, J., Benn, K., and Rimando, R.E. 1995. Recent, tectonically induced, surficial stress-relief structures in the Ottawa–Hull area, Canada. *Canadian Journal of Earth Sciences*, **32**(3): 325–333. doi:10.1139/e95-027.
- Walters, R.J., Elliott, J.R., D’agostino, N., England, P.C., Hunstad, I., Jackson, J.A., et al. 2009. The 2009 L’Aquila earthquake (central Italy): a source mechanism and implications for seismic hazard. *Geophysical Research Letters*, **36**(17). doi:10.1029/2009GL039337.
- Wang, J., Xu, C., Freymueller, J.T., Li, Z., and Shen, W. 2014. Sensitivity of Coulomb stress change to the parameters of the Coulomb failure model: a case study using the 2008 M_W 7.9 Wenchuan earthquake. *Journal of Geophysical Research: Solid Earth*, **119**(4): 3371–3392. doi:10.1002/2012JB009860.
- Wells, D.L., and Coppersmith, K.J. 1994. New empirical relationships among magnitude, rupture length, rupture width, rupture area, and surface displacement. *Bulletin of the Seismological Society of America*, **84**(4): 974–1002. doi:10.1785/BSSA0840040974.
- Xu, H., Xu, S., Nieto-Samaniego, Á.F., and Alaniz-Álvarez, S.A. 2017. Slicken 1.0: program for calculating the orientation of shear on re-activated faults. *Computers and Geosciences*, **104**: 158–165. doi:10.1016/j.cageo.2016.07.015.
- Yu, K., Chouinard, L.E., and Rosset, P. 2016. Seismic vulnerability assessment for Montreal. *Georisk: Assessment and Management of Risk for Engineered Systems and Geohazards*, **10**(2): 164–178. doi:10.1080/17499518.2015.1106562.
- Ziv, A., and Rubin, A.M. 2000. Static stress transfer and earthquake triggering: no lower threshold in sight? *Journal of Geophysical Research*, **105**(B6): 13631–13642. doi:10.1029/2000JB900081.